Structural basis for the assembly and modulation of human M-channels

Fangzhou Lu[1,2,4], Xiaoshuang Huang[1,4], Guanxing Cai[3], Yuzhen Xie[1], Xiao Fan[1,5], and Jian Huang[1,5]

[1]Institute of Bio-Architecture and Bio-Interactions (IBABI), Shenzhen Medical Academy of Research and Translation (SMART), Shenzhen 518107, Guangdong, China.

[2]Westlake University, Hangzhou 310024, Zhejiang, China.

[3]Biomedical Electrophysiology Core Facility, Shenzhen Medical Academy of Research and Translation (SMART), Shenzhen 518107, Guangdong, China.

[4]These authors contributed equally: Fangzhou Lu, Xiaoshuang Huang.

[5]To whom correspondence should be addressed: Jian Huang (huangjian@smart.org.cn); Xiao Fan (xfan@smart.org.cn).

Abstract

Human M-channels, primarily assembled by heteromeric KCNQ2/KCNQ3 subunits, are critical regulators of neuronal excitability, and loss-of-function mutations in either subunit are linked to epileptic disorders. Yet, the molecular mechanisms underlying heteromeric assembly, gating, and pharmacological modulation have remained largely elusive. Here, we present high-resolution cryo-EM structures of human M-channels in apo and activator-bound states, revealing a dominant asymmetric 3:1 and a minor staggered 2:2 stoichiometry of KCNQ2 to KCNQ3, with consistent ratios across datasets. We further examine the mechanisms of action (MOAs) of two distinct modulators: ICA-110381 selectively engages and stabilizes activated KCNQ2 voltage sensors, whereas XEN1101 occupies pore fenestrations and promotes channel opening through a PIP_2-assisted cooperative gating process. Electrophysiological analyses corroborate these observations, establishing the basis for subtype-selective modulation, cooperative gating, and KCNQ3-driven low-voltage activation. Together, our findings provide a foundation for interpreting pathogenic mutations and advancing the rational design of next-generation antiepileptic therapeutics targeting the M-channels.

Introduction

Voltage-gated potassium channels of the KCNQ family (KCNQ1-5) are widely expressed in excitable tissues, where they shape action potentials by driving repolarization and stabilizing the resting potential[1-3]. Individual isoforms exhibit distinct tissue distributions: KCNQ1 predominates in the heart, kidney, and cochlea[2,4], KCNQ4 is restricted to inner ear hair cells and certain brainstem regions involved in auditory modulation[5,6], and KCNQ2, KCNQ3, and KCNQ5 are enriched in the central nervous system[1,7-9]. Among neuronal channels, KCNQ2 and KCNQ3 form homo- and hetero-tetramers that primarily mediate the non-inactivating M-current, a key regulator of neuronal excitability at the axon initial segment and nodes of Ranvier[9-14]. Notably, heteromeric KCNQ2/KCNQ3 channels generate substantially larger currents than either homomer, highlighting their crucial physiological and therapeutic relevance[10,12,13,15].

Structurally, KCNQ channels adopt a canonical domain-swapped architecture with four independent subunits, each containing six transmembrane helices (S1-S6). The S5 and S6 segments from all subunits assemble into the central pore domain (PD), while S1–S4 constitute the peripheral voltage-sensing domains (VSDs)[2,16-19]. Recent cryo-EM studies have resolved several homomers, including KCNQ1, KCNQ2, KCNQ4, and KCNQ5[20-27], and uncovered modulatory roles of auxiliary subunits such as KCNE1/3[4,18,28,29], the chaperone calmodulin (CaM)[17,30-32], the endogenous lipid phosphatidylinositol 4,5-bisphosphate (PIP_2)[23,27,33,34], and a range of pharmacological agents[20-27,35,36]. By contrast, the structural organization and pharmacological modulation of heteromeric M-channels, especially the

physiologically dominant KCNQ2/KCNQ3 complex, remain poorly understood. The stoichiometry of heteromeric M-channel assembly has long been a key question in the field.

Loss-of-function mutations in KCNQ2 or KCNQ3 are associated with certain types of epileptic disorders, including KCNQ2-related developmental and epileptic encephalopathy (DEE7)[37,38] and benign familial neonatal seizures (BFNS1/2)[39-41]. More than 80 pathogenic variants have been identified, underlining the critical role of M-channels in maintaining cortical excitability[30,42,43]. Enhancing the M-current pharmacologically has long been pursued for epilepsy treatment. Retigabine, the first FDA-approved KCNQ channel opener, potentiated M-channel activity but was ultimately withdrawn due to adverse effects such as retinal pigmentation and urinary retention[44-46]. These complications arose from off-target activation of retinal or bladder KCNQ isoforms, emphasizing the urgent need for subtype-selective modulators.

Recent efforts have yielded promising next-generation KCNQ modulators with improved specificity and safety profiles. XEN1101 (Azetukalner), a pore-targeting KCNQ2/3-selective opener, has demonstrated sustained seizure-reducing efficacy in phase IIb trials, without requiring titration or causing pigmentary abnormalities[47-49]. ICA-110381, by contrast, is a KCNQ2-specific activator with anticonvulsant properties that targets voltage sensors, providing a mechanistically distinct route to channel opening[22,50]. Concurrently, drug repurposing efforts have highlighted variant- and isoform-specific effects of compounds such as gabapentin and donepezil on KCNQ channels[36,51], reinforcing the therapeutic potential of

subtype-selective agents to avoid off-target effects while addressing drug-resistant epilepsy.

Here, we reported cryo-EM structures of heteromeric human M-channels in both apo and activator-bound states at high resolutions of 2.4-3.0 Å. Combined with functional assays, these structures revealed how XEN1101 and ICA-110381 engage distinct binding modes to stabilize activated 'up' VSDs. We further uncovered a stepwise gating mechanism in which PD-targeting modulators act cooperatively with PIP_2 binding at the VSD-PD interface to reinforce conformational transitions and promote pore opening. Together, these findings provided the structural basis of cooperative gating in heteromeric M-channels and established a mechanistic framework for subtype-specific pharmacology, with direct implications for the treatment of epilepsy and related channelopathies.

Results

Structural and functional characterization of heteromeric M-channels

To reconstruct heteromeric M-channels, we first co-expressed codon-optimized full-length KCNQ2 (Uniprot O43526) and KCNQ3 (Uniprot O43525) with distinct C-terminal affinity tags (Fig. S1). Whole-cell patch-clamp recordings in HEK293T cells confirmed that co-expression produced robust heteromeric currents, with amplitudes substantially larger than those generated by either subunit alone (Fig. S2a,b and Table S1).

Using tandem affinity purification, we isolated channel complexes containing both KCNQ2 and KCNQ3 subunits. However, the low expression level initially limited cryo-EM

particle collections. Guided by prior work on homomeric KCNQ structures, we truncated disordered regions at both termini to improve protein stability and yield[24-26]. The truncated constructs indeed expressed at higher levels and retained gating properties comparable to wild-type channels (Fig. 1a-c).

Following well-established protocols for protein purification, cryo-sample preparation, data acquisition, and processing, we obtained high-resolution three-dimensional reconstructions of heteromeric KCNQ2/KCNQ3 channels at 2.4-2.7 Å (Figs. S2-S4 and Table S2). Although calmodulin (CaM) was not co-expressed, densities corresponding to endogenous CaM were observed bound to the intracellular HA-HB hairpin, consistent with prior co-expression structures[17,21,26]. For consistency, no exogenous CaM was introduced in subsequent preparations. Meanwhile, this association imposed an asymmetric arrangement, with one CaM-binding hairpin poorly resolved and the HC coiled-coil displaced from the central axis, resulting in a reduced resolution in the cytoplasmic region (Figs. 1d and S4b). Accordingly, our analysis focused primarily on the transmembrane regions.

The transmembrane domain was resolved at sufficient resolution to permit reliable atomic modeling. The heteromeric KCNQ2/KCNQ3 complex adopts the canonical domain-swapped architecture of voltage-gated potassium channels. Distinct side-chain signatures — including Tyr284 in KCNQ2 versus Thr323 in KCNQ3 near the extracellular vestibule, Tyr226 versus Cys255 on the S4-5 linker, and differences in extracellular loops (KCNQ2: residues 255-263, 8 aa; KCNQ3: residues 284-302, 18 aa) — enabled unambiguous subunit

assignment (Fig. S4c-h). These identifiers revealed a predominant asymmetric 3:1 stoichiometry of three KCNQ2 subunits paired with one KCNQ3 (84%), along with a minor staggered 2:2 assembly (16%) reconstructed at lower resolution (Figs. 1d,e and S4c). Subsequent analyses focused on the high-quality asymmetric 3:1 complex. For clarity, the three KCNQ2 subunits in this assembly were designated $KCNQ2_{I}$, $KCNQ2_{II}$, and $KCNQ2_{III}$ in counterclockwise order from the unique KCNQ3 when viewed from the extracellular side, and the heteromeric KCNQ2/KCNQ3 complex is hereafter referred to as the M-channel.

Structural differences between KCNQ2 and KCNQ3 subunits

To dissect the structural determinants underlying subunit heterogeneity, we sought to resolve the cryo-EM structures of homotetrameric KCNQ2 and KCNQ3 channels using the same engineered constructs. While poor sample quality limited high-resolution reconstruction of KCNQ3, KCNQ2 was determined at 2.3 Å (Fig. S5 and Table S2). Comparison of the M-channel with homomeric KCNQ2 revealed pronounced conformational differences attributable to KCNQ3, most notably a counterclockwise rotation of the KCNQ3 VSD when viewed extracellularly (Fig. 2a).

The selectivity filter (SF) of the M-channel preserved the canonical TIGYG motif that coordinates a linear array of four K^+ ions, closely resembling that of homotetrameric KCNQ2[19,20,22]. However, sequence alignment across the KCNQ family revealed a notable divergence: KCNQ3 harbors a unique alanine immediately preceding the TIGYG motif, whereas other subtypes, including KCNQ2, contain a conserved threonine (Figs. 2b and S1).

Electrophysiological analysis confirmed this site as a key determinant of subtype-specific activity. The KCNQ3 A315T mutation produced robust currents that even exceeded those of co-expressed KCNQ2 and KCNQ3, consistent with earlier reports[12,52,53]. Conversely, substitution of threonine with alanine at the equivalent position in KCNQ2 (T276A) significantly diminished currents (Figs. 2c and S6a), a phenotype reminiscent of the pathogenic T276I variant associated with Ohtahara syndrome (early infantile developmental and epileptic encephalopathy, EIDEE)[54,55].

Within the VSD, additional differences were observed. The S4 helix of KCNQ3 adopted a more activated 'up' conformation, and an elongated loop spanning Arg227-Phe231 replaced the helical turn in KCNQ2 (Fig. 2d,e). Previous studies have suggested that the M-channel exhibits unique low-voltage activation, potentially arising from this activated VSD[56,57]. To test this, we designed a chimeric channel combining the PD of KCNQ2 with the VSD of KCNQ3. Expression of this chimera, either alone or co-expressed with wild-type KCNQ3, induced a pronounced hyperpolarizing shift in activation, with half-activation voltages ($V_{1/2}$) of -35.32 ± 1.71 mV and -33.85 ± 0.62 mV, respectively (Figs. 2f and S6b). These results indicated that KCNQ3 contributes to heteromeric M-channel function primarily by tuning voltage dependence via its VSD, rather than forming a functional homomeric channel.

Together, these structural and functional analyses define how unique molecular features of KCNQ3 shape the function of heteromeric M-channels. Beyond intrinsic subunit

composition, M-channel activity is further modulated by pharmacological modulators. We next examined two mechanistically distinct activators: the VSD-targeting ICA-110381 and the PD-targeting XEN1101 (Azetukalner), the latter currently in phase III clinical trials.

ICA-110381 selectively targets the KCNQ2 VSD

ICA-110381, a small-molecule M-channel activator with anticonvulsant properties, potentiated current amplitude and attenuated tail-current inactivation in a dose-dependent manner (Fig. S7a,b). This effect was accompanied by an induced hyperpolarizing shift in voltage-dependent activation, with $V_{1/2}$ moving from -24.71 ± 0.54 mV to -49.27 ± 0.65 mV, yielding an EC_{50} of 1.81 ± 0.29 μM (Fig. 3a). Notably, ICA-110381 exhibited pronounced subtype selectivity: at 10 μM, it shifted KCNQ2 activation leftward by $\Delta V_{1/2}$ of -32.20 ± 2.19 mV, while KCNQ3 remained largely unaffected (Figs. 3b, S7b, and S7c).

To elucidate the structural basis of this selectivity, we determined cryo-EM structures of ICA-110381-bound M-channels in multiple conformations at 2.8-3.0 Å resolutions (Fig. S8a-d). Additional densities were immediately identified within the cavities of KCNQ2 VSDs, but not KCNQ3, providing direct evidence of subtype-specific engagement (Fig. 3c-e). Model building revealed ICA-110381 resided in a hydrophobic cavity of the KCNQ2 VSD, coordinated by Ile134 and Phe137 on S2, Phe168, Ile171, Asp172, Val175, and Leu176 on S3, and Leu206, Arg207, Ile239, and Arg210 on S4 (Fig. 3f, *left*). Following our recently proposed nomenclature for drug-binding sites on voltage-gated ion channels, this site is designated site VC, referring to the **c**avity of **V**SD[19].

Sequence alignment further illuminated the molecular determinants of this specificity. In KCNQ2, residues Phe168 and Ile171 on S3, together with Ile209 on S4, shaped the hydrophobic cavity that accommodates ICA-110381. In KCNQ3, the corresponding residues — Leu198, Leu201, and Leu238 — altered side-chain geometry, disrupting steric complementarity (Fig. 3f, *right*). Particularly, Phe168 in site VC forms a π–π stacking interaction with the aromatic ring of ICA-110381, a stabilizing feature absent in KCNQ3 due to the leucine substitution. These variations explain the structural incompatibility of KCNQ3 with ICA-110381.

Binding of ICA-110381 also triggered conformational rearrangements within KCNQ2 VSDs. In a representative extracellular view, the VSD underwent a counterclockwise rotation, bringing S4 closer to the pore-forming S5 helix and strengthening interdomain contacts. This arrangement was observed across all KCNQ2 VSDs, although the angle varied slightly in $KCNQ2_I$ and $KCNQ2_{II}$ (Figs. 3g, *upper* and S8e). Concurrently, ICA-110381 stabilized S4 in an ‘up’ conformation relative to the apo state (Fig. 3g, *lower* and 3h). This stabilization mirrors the mechanism proposed for ztz240, in which ligand binding traps the VSD in an activated state, strengthens VSD-PD coupling, and promotes channel opening[22,24]. Together, these results demonstrate that ICA-110381 activates M-channels by selectively stabilizing the activated KCNQ2 VSDs, conferring subunit-specific modulation within heteromeric assemblies.

XEN1101 engages all four fenestrations of the PD

XEN1101 (Azetukalner) is a next-generation small-molecule opener of neuronal KCNQ channels, currently in late-stage clinical development for focal epilepsy and other seizure disorders[47-49]. As a derivative of retigabine, the first FDA-approved KCNQ channel modulator, XEN1101 was rationally designed to circumvent the metabolic instability and adverse effects of its predecessor[58]. Functionally, XEN1101 induced a significant hyperpolarizing shift in channel activation, moving the $V_{1/2}$ from -22.83 ± 0.58 mV to -67.61 ± 4.44 mV, with an EC_{50} of 0.66 ± 0.13 μM (Figs. 4a and S9).

Following the same strategy applied to apo and ICA-110381-bound complexes, we determined the high-resolution cryo-EM structures of the M-channel in complex with XEN1101 (Fig. S10a,b). The densities were well-resolved, enabling unambiguous modelling of both the channel and the bound ligands (Figs. 4b, S3 and S10c-e, and Table S2). Similar to retigabine, XEN1101 occupied all four fenestrations of the PD through a conserved binding pose, regardless of the specific KCNQ subunit composition[21,22]. Each pocket was enclosed by the S5 and S6 helices of adjacent subunits and the S4–S5 linker of one contributing subunit (Fig. 4c,d).

Detailed inspection of heteromeric KCNQ2-KCNQ3 interfaces revealed a highly conserved binding pattern. At the interface between $KCNQ2_{III}$ and KCNQ3, the pocket was composed of residues Leu299, Ile300, Ser303, and Phe304 on S6 of $KCNQ2_{III}$, together with Leu250 and Ile254 on the S4-5 linker of KCNQ3, Trp265, Phe269, and Leu272 on its S5

helix, and Phe344, Pro347, and Leu351 on its S6 helix (Fig. 4e, *left*). This predominantly hydrophobic cavity was well-suited for ligand accommodation. Within this pocket, the amide group of XEN1101 engaged in two stabilizing hydrogen bonds — one with the backbone carbonyl of Leu299 in $KCNQ2_{III}$ and another with the indole nitrogen of Trp265 in KCNQ3. In addition, the aromatic core of XEN1101 formed π–π stacking with Trp265 of KCNQ3, further stabilizing ligand binding. A similar binding pattern was observed at the second heteromeric interface between KCNQ3 and $KCNQ2_{I}$, with only one difference: Ile254 in KCNQ3 was replaced by Val225 in $KCNQ2_{I}$, slightly altering the hydrophobic contact with the 3,3-dimethylbutanoyl tail of XEN1101 but leaving overall binding largely unaffected (Fig. 4e, *right*). This conservation across interfaces explained the nearly equivalent occupancy of XEN1101 at all four PD fenestrations.

Ligand binding was also accompanied by local conformational adjustments, most notably in the indole-bearing tryptophan residues. Trp236 in KCNQ2, or the corresponding Trp265 in KCNQ3, underwent a pronounced rotation to enable π–π stacking with XEN1101. A subtle outward displacement of the neighboring S6 helix further expanded the pocket, optimizing ligand accommodation (Fig. 4f). Collectively, these structural adaptations highlighted a conserved PD-binding mode of XEN1101 on heteromeric M-channels.

Cooperative gating induced by PD-targeting modulators

Beyond retigabine, the MOAs for several PD-targeting KCNQ activators, including cannabidiol (CBD), HN37, Ebio1, and QO-83 (PDB: 8XO1), have been elucidated in

homomeric channels[24,25]. In addition to these exogenous agents, endogenous cofactors are essential for channel activation, particularly CaM and PIP_2. PIP_2 binding is critical for channel opening, and its depletion by phospholipase C rapidly suppresses M currents[57]. Although we did not capture the M-channel in an open state simultaneously bound to XEN1101 and PIP_2, the heteromeric assemblies provided unique insights into their synergistic action. Unlike the synchronous activation of homomeric channels, the heteromeric M-channel exhibits a distinctive cooperative gating mode.

Despite the conserved occupancy of all four fenestrations by XEN1101, multiple XEN1101-bound states were resolved at high resolutions of 2.5-2.7 Å. Only the reconstruction in which all four VSDs adopted the 'up' conformation was obtained at lower resolution, owing to limited particle numbers (Table S2). Notably, all structures maintained the predominant 3:1 stoichiometry of KCNQ2 to KCNQ3 (Fig. S10b), as confirmed by the abovementioned signature residues and subtype-specific features of the S4 helices. Conformational changes induced by XEN1101 occurred exclusively in KCNQ2 subunits, rather than reflecting altered channel composition (Fig. 5a).

Viewed from the extracellular side, the three KCNQ2 VSDs rotated sequentially in a counterclockwise order: $KCNQ2_I$ rotated first, followed by the neighboring $KCNQ2_{II}$, and then $KCNQ2_{III}$. These intermediate states, designated State 1-4, represent progressive stages of VSD transition (Fig. 5a and Movie S1). Despite their closed PDs, the VSD rearrangements closely resembled those observed in homomeric KCNQ2 bound to HN37 and PIP_2, where the

pore is open (Fig. 5a, *right*). These observations suggest that the heteromeric M-channel activates through a stepwise, cooperative process.

Closer inspection of the PD-VSD interfaces revealed that ligand occupancy critically modulates coupling. In apo M-channels, two unidentified sterol-like densities were consistently observed at the interface between the KCNQ2 VSD and pore, but were absent from the KCNQ3 VSD-PD interface. These densities, designated ligand-a (intracellular side) and ligand-b (extracellular side), appeared to tether the VSD to the PD (Fig. 5b). Upon XEN1101 binding, ligand-b densities were displaced by steric exclusion, with the site occupied by XEN1101 and nearby residues including $Trp288_{III}$, $Ile115_{I}$, and $Glu117_{I}$ (Fig. 5c). As VSD rotation progressed, the density of ligand-a disappeared, and S4 adopted an activated 'up' conformation similar to that of KCNQ3, with S1 moving outward from the PD (Fig. 5b,d). This reorganization created a lipid-accessible cavity formed by S1, S4, and S6 of one subunit and S5 and the S4-5 linker of the neighbor, providing an ideal pocket for PIP_2 accommodation (Fig. 5b). In the open KCNQ2 structure, PIP_2 stabilized this interface through hydrogen bonds with Arg87 on S1, Arg214 on S4, Lys327 on S6, and Lys230 on S5 of the adjacent subunit, reinforcing VSD-PD coupling and promoting outward movement of the S6 helices to open the pore (Fig. 5e)[24].

Together, these structural snapshots demonstrated a cooperative mechanism for M-channel activation. Binding of exogenous PD-targeting activators perturbed lipid interactions at the VSD-PD interface, initiating sequential VSD rotations and creating a permissive pocket

for PIP_2 engagement. PIP_2 then reinforced VSD-PD coupling and drove splaying of the S6 helices, culminating in pore opening. In contrast to the synchronous transitions of homomeric channels, heteromeric M-channels underwent sequential conformational changes across KCNQ2 subunits, providing mechanistic insights into cooperative gating (Fig. 5f). While the precise temporal order of PIP_2 engagement remained unresolved, the present structures provided critical intermediates and mechanistic evidence for cooperative opening in heteromeric M-channels.

Discussion

This study aimed to address the central question in the KCNQ field: how the molecular architecture of heteromeric M-channels underlies their physiological dominance and therapeutic relevance. High-resolution cryo-EM structures of KCNQ2/3 assemblies, combined with functional analyses, revealed a predominant asymmetric 3:1 stoichiometry of KCNQ2 to KCNQ3, alongside a minor but stable staggered 2:2 population. Strikingly, this compositional heterogeneity (78%-84% 3:1 stoichiometry across conditions) was consistently observed across apo, ICA-110381-bound, and XEN1101-bound datasets, and the selective engagement of KCNQ2-targeting modulator ICA-110381 directly validated both assemblies. Theoretically, if the two distinct subunits were incorporated randomly, the stoichiometries would follow a binomial distribution. However, the absence of other stoichiometries, including the neighboring 2:2 form, argues against stochastic incorporation and instead implies a regulated assembly process driven by intrinsic subunit features. While the asymmetric 3:1 form accounted for the majority of particles, the staggered 2:2 assembly

remained functionally competent, as evidenced by the selective binding of ICA-110381 to diagonally opposed KCNQ2 VSDs. The coexistence of these two defined architectures suggests that neuronal excitability is supported by a balance of different assemblies, with modulators engaging them in distinct ways.

Our findings further delineate subunit-specific contributions to M-channel function. KCNQ3 uniquely harbors an alanine preceding the selectivity filter that alters conductance in homomeric channels, while its pre-activated voltage sensors lower the activation threshold of heteromers. KCNQ2, in contrast, provides a unique pharmacological scaffold, with ICA-110381 engaging exclusively hydrophobic pockets in KCNQ2 VSDs. Co-expression of KCNQ2 and KCNQ3 yielded robust currents larger than either homomer alone, indicating the physiological necessity of heteromeric assembly. This division of labor between KCNQ2 and KCNQ3 explains why heteromeric M-channels outperform homomers in regulating neuronal excitability and highlights the emergent properties arising from heteromerization.

The structures also provide a mechanistic interpretation of disease mutations. Mapping pathogenic variants onto heteromeric M-channels revealed a striking convergence of DEE- and BFNS-associated mutations on residues within the P-loop and voltage sensors, particularly the signature SF motif and gating-charge residues essential for ion permeation and gating transitions (Fig. S11 and Table S3). Perturbations at these sites likely destabilize pore architecture or impair voltage sensing, leading to reduced M-current and neuronal hyperexcitability. Mutations within the VSD-PD interface, including those directly involved

in PIP_2 recruitment such as R214W in KCNQ2, may instead abolish PIP_2-mediated coupling (Fig. S11). These observations not only clarify how diverse mutations converge on common structural hotspots but also suggest opportunities for genotype-tailored therapies, in which modulators could be selected to compensate for specific structural defects.

Our results also expand the pharmacological landscape of M-channel modulation. ICA-110381 engages a unique hydrophobic pocket within KCNQ2 VSDs, stabilizing the activated conformation and establishing a paradigm for subtype-selective modulation. By contrast, XEN1101 exploits a cooperative gating mechanism, progressing through multiple conformational intermediates. Binding of XEN1101 within PD fenestrations displaces sterol-like lipids, triggers sequential VSD rotations, and reorganizes the PD-VSD interface to favor PIP_2 recruitment. PIP_2, in turn, reinforces interdomain coupling through conserved basic residues, driving outward splaying of the S6 helices and promoting pore opening. This lipid-drug cooperativity likely represents a general mechanism for pharmacological regulation in heteromeric ion channels, where endogenous lipids tune the efficacy of exogenous modulators.

In summary, our study establishes the structural basis of heteromeric M-channel assembly, cooperative gating, and pharmacological modulation. By integrating stoichiometric heterogeneity, subunit-specific contributions, and disease-mutation mapping, we provide a mechanistic framework bridging molecular architecture to neuronal excitability and epilepsy. Beyond fundamental insights, the structural elucidation of KCNQ2-specific sites lays the

groundwork for rational design of subunit-selective modulators, paving the way for precision therapies for KCNQ-related channelopathies.

Methods

Cell culture and transient expression of human KCNQ subunits in HEK293F cells

HEK293F suspension cells (gift of Sino Biological Inc.) were maintained in SMM 293T-II medium (Sino Biological Inc.) at 37 °C under 5% CO_2 and 60% humidity.

Codon-optimized cDNAs encoding full-length human KCNQ2 (Uniprot O43526) and KCNQ3 (Uniprot O43525) were synthesized (BGI Geneland Scientific, Shenzhen) and cloned into the pCAG vector separately with a FLAG-tag and Twin-Strep-tag at the C-terminus, respectively. To improve expression, engineered constructs were generated by truncation based on previous work, yielding $KCNQ2^{EM}$ (Ala62-Ser672) and $KCNQ3^{EM}$ (Ala89-Ser665), each comprising the S0-S6 transmembrane segments with flanking intracellular helices[25]. All plasmids intended for transient expression were verified through DNA sequencing.

Cells were transfected at a density of 1.5-2.0 × 10^6 cells per mL. For each one-liter cell culture, a mixture of 1.5 mg expression plasmids of heteromeric KCNQ, including 0.75 mg each of KCNQ2 and KCNQ3, were pre-incubated with 3 mg 40-kDa linear polyethylenimines (Hieff Trans®PEI MW40000, YEASEN) in 50 mL fresh medium for 15-30 minutes before adding to the culture. Recombinant co-expression of KCNQ2/3 complexes was achieved under these conditions.

Protein purification of human KCNQ2/KCNQ3 complexes

At approximately 48 h after transfection, 12 L of transfected HEK293F cells were harvested by centrifugation at 3,600 g for 10 min and resuspended in the lysis buffer containing 25 mM HEPES (pH 7.4), 150 mM KCl, protease inhibitor cocktails (SelleckChem), and 1 mM phenylmethanesulfonyl fluoride (PMSF, Sigma-Aldrich). The suspension was homogenized and then supplemented with n-dodecyl-β-D-maltopyranoside (DDM, Anatrace) to a final concentration of 1% (w/v) and cholesteryl hemisuccinate Tris salt (CHS, Anatrace) to 0.1% (w/v). After incubation at 4 °C for 2 h, the mixture was centrifuged at 32,000 g for 45 min, and the supernatant was applied to the anti-Flag M2 affinity gel (Sigma) for affinity purification. The resin was rinsed twice with 5 column volume (CV) buffer A, which contains 25 mM HEPES (pH 7.4), 150 mM KCl, 0.06% (w/v) DDM, and 0.006% (w/v) CHS, as well as protease inhibitor cocktails, and rinsed three times with 2 CV buffer B, which contains a different detergent by 0.06% (w/v) GDN. Target proteins were eluted with 6 CV buffer B supplemented with 0.4 mg/mL FLAG peptide. The eluent was then applied to Strep-Tactin Sepharose (IBA) and allowed to flow through by gravity. The target proteins were eluted with buffer B supplemented with 2.5 mM desthiobiotin (IBA). The eluent was then concentrated using 100-kDa molecular weight cut-off Amicon filter units (Millipore) and subjected to size-exclusion chromatography (Superose 6 Increase 10/300 GL column, GE Healthcare) pre-equilibrated with running buffer containing 25 mM HEPES (pH 7.4), 150 mM KCl, and 0.02% GDN. Peak fractions were pooled and concentrated to 4-6 mg mL^{-1}.

For preparation of ligand-bound complexes, XEN1101 and ICA-110381 stocks in DMSO (MCE) were diluted with gel filtration buffer and mixed with purified protein at a final

concentration of 1 mM. All the mixtures were incubated at 4 °C for 30 min before cryo-grid preparation.

Cryo-EM sample preparation and data acquisition

Ni-Ti grids (M01-Au300-R1.2/1.3, Nano Dimension Ltd.) were glow-discharged before use. Freshly purified M-channel complexes, with or without ligands, were applied to grids in a Vitrobot Mark IV chamber operated at 8 °C and 100% humidity. After blotting for 3.5 seconds, grids were plunge-frozen into liquid ethane and cooled by liquid nitrogen.

Data were collected on a 300 kV Titan Krios G4 cryogenic electron microscope (Thermo Fisher), equipped with a Gatan K3 direct electron detector and a GIF Quantum energy filter. Micrographs were captured using Falcon IVi (Thermo Fisher) in EC mode at a nominal magnification of 130,000×, corresponding to a calibrated pixel size of 0.936 Å. Data were acquired at a preset defocus range of -1.2 μm to -1.6 μm. Each EER-format movie stack was exposed within a 0.79-μm spot size and accumulated a total electron dose of approximately 50 $e^{-}/Å^{2}$ in EPU (Thermo Fisher). Subsequently, the movie stacks underwent alignment, summation, and dose-weighting using cryoSPARC live[59].

Cryo-EM data processing

A total of 5,578/6,443/5,745/6,852 cryo-EM micrographs were collected for KCNQ2/KCNQ3-apo/ICA-110381/XEN1101 and KCNQ2 homomer, respectively. During cryoSPARC live preprocessing, patched CTF estimation was implemented. For the

KCNQ2/KCNQ3-apo dataset, 787,548 particles were picked using a pre-trained general Topaz model[60], and subsequent 2D classification was performed with extracted bin-2 particles. Particles from good 2D Class averages with clear secondary structure features are used for *ab initio* reconstruction. The resulting 280,040 particles from the best 3D reconstruction were selected for another round of 2D Classification. The best particles after 2D classification were used to train a new Topaz model, which re-picked 1,560,372 particles from the collected micrographs. The new set of bin-2 particles undergoes multiple rounds of 2D classification and continuous heterogeneous refinement. Subsequently, 1,184,540 particles were re-extracted into bin-1 and underwent three additional rounds of heterogeneous refinement, yielding a 2.4 Å NU-refinement reconstruction in a mixed conformation. To resolve the conformational heterogeneity, we conducted 3D variability analysis and reference-free 3D classification on the selected 789,952 particles. The resulting representative classes were used as references for further heterogeneous refinement, followed by NU-local refinement. This workflow successfully separated the particles into distinct classes corresponding to different VSD conformations. A similar workflow was applied to the KCNQ2/KCNQ3-ICA-110381/XEN1101 datasets.

Model building and refinement

The initial models for KCNQ in different complexes were adapted from the apo-state homo-tetrameric KCNQ2 structure (PDB: 7CR3) and underwent manual inspection and adjustments in COOT[61], with the 3D structures of the ligands (XEN1101 and ICA110381) being docked and refined based on the density. Refinement against the corresponding map was carried out

using the Real-space Refinement option in PHENIX[62]. Further structure optimization was performed with ISOLDE[63], followed by a final round of Real-space Refinement in PHENIX[62]. Detailed validation results for the model refinement are provided in Table S2.

Whole cell electrophysiology

HEK293T cells were plated onto glass coverslips and transiently co-transfected with 1 μg expression plasmid (0.5 μg each plasmid of KCNQ2 and KCNQ3 for co-transfection) and 0.1 μg eGFP, using Lipofectamine 3000 (Invitrogen). Whole-cell patch-clamp recording for GFP-positive cells was performed at room temperature after 18 h of transfection.

The whole-cell potassium currents were recorded using an EPC10-USB amplifier with Patchmaster software v2*73.5 (HEKA Elektronic), sampled at 10 kHz and filtered at 2.9 kHz (low-pass Bessel). The external solution contained (in mM) 140 NaCl, 5 KCl, 1 $MgCl_2$, 2 $CaCl_2$, 10 Glucose, and 10 HEPES (pH 7.4). The internal solution contained (in mM) 145 KCl, 10 HEPES, 5 EGTA, and 2 Mg-ATP (pH 7.4). Borosilicate pipette electrodes (Sutter Instrument) with a resistance of 2-4 MΩ were used.

To obtain the voltage-dependent activation curves, cells were stepped from a -80 mV holding potential to voltages ranging from -90 mV to +70 mV for 1500 ms in 10 mV increments. Tail currents were then recorded at -120 mV for 500 ms (Fig. S2a). Tail peak currents were measured to reflect conductance (G) at different applied voltage steps. Conductance activation curves were fitted to a Boltzmann equation: $G/G_{max} = 1/\{1 + \exp[(V_{1/2} - V_m)/slope]\}$, where G_{max} is the maximal conductance, $V_{1/2}$ is the half-activation potential, V_m

is the membrane potential, and slope is the slope factor.

For assessing the effects of ICA-110381 and XEN1101, cells were stepped from a -100 mV holding potential to voltages ranging from -110 mV to +50 mV for 1500 ms in 10 mV increments. Tail currents were then recorded at -120 mV for 500 ms. During the experiments, the bath solution was continuously perfused by a gravity-perfusion system (ALA Scientific Instruments), and the compound solutions were perfused for several minutes to achieve steady effect. Concentration-response curves were fitted using the equation Y = Bottom+ (Top - Bottom) / (1 + 10^((LogEC_{50}-X) * Hill Slope)), where Y represents the shifts of $V_{1/2}$ of the Boltzmann relationship for the voltage-dependent activation induced by different compound concentrations, EC_{50} is the concentration of the compound that activated 50% of the max change in $V_{1/2}$ and X denoted the log of concentration, and Hill Slope indicated the slope factor. The effect of ICA-110381 on KCNQ2, KCNQ3, and KCNQ2/3 was quantified by the shifts in $V_{1/2}$ at 10 μM, respectively.

To evaluate the conductivity of different modified proteins, current density was calculated by measuring tail peal currents in response to +50 mV voltage steps, followed by normalization to cell capacitance (pA/pF).

Data were analyzed using Fitmaster (HEKA Elektronik), Origin (OriginLab), and GraphPad Prism (GraphPad Software). All data points are presented as mean ± SEM, with n indicating the number of experimental cells. Statistical significance was assessed using unpaired t-tests,

one-way ANOVA analysis, and extra sum-of-squares F tests.

Data availability

The data that support this study are available from the corresponding authors upon reasonable request. The cryo-EM maps and corresponding atomic coordinates have been deposited in the Electron Microscopy Data Bank (EMDB) and the Protein Data Bank (PDB).

Reference

1 Barrese, V., Stott, J. B. & Greenwood, I. A. KCNQ-Encoded Potassium Channels as Therapeutic Targets. *Annu Rev Pharmacol Toxicol* **58**, 625-648 (2018). https://doi.org/10.1146/annurev-pharmtox-010617-052912

2 Abbott, G. W. KCNQs: Ligand- and Voltage-Gated Potassium Channels. *Front Physiol* **11**, 583 (2020). https://doi.org/10.3389/fphys.2020.00583

3 Cooper, E. C. & Jan, L. Y. M-channels: neurological diseases, neuromodulation, and drug development. *Arch Neurol* **60**, 496-500 (2003). https://doi.org/10.1001/archneur.60.4.496

4 Agsten, M. *et al.* BACE1 modulates gating of KCNQ1 (Kv7.1) and cardiac delayed rectifier KCNQ1/KCNE1 (IKs). *J Mol Cell Cardiol* **89**, 335-348 (2015). https://doi.org/10.1016/j.yjmcc.2015.10.006

5 Kubisch, C. *et al.* KCNQ4, a novel potassium channel expressed in sensory outer hair cells, is mutated in dominant deafness. *Cell* **96**, 437-446 (1999). https://doi.org/10.1016/s0092-8674(00)80556-5

6 Kharkovets, T. *et al.* KCNQ4, a K+ channel mutated in a form of dominant deafness, is expressed in the inner ear and the central auditory pathway. *Proc Natl Acad Sci U S A* **97**, 4333-4338 (2000). https://doi.org/10.1073/pnas.97.8.4333

7 Brown, D. A. & Adams, P. R. Muscarinic suppression of a novel voltage-sensitive K+ current in a vertebrate neurone. *Nature* **283**, 673-676 (1980). https://doi.org/10.1038/283673a0

8 Jentsch, T. J. Neuronal KCNQ potassium channels: physiology and role in disease. *Nat Rev Neurosci* **1**, 21-30 (2000). https://doi.org/10.1038/35036198

9 Wang, J. J. & Li, Y. KCNQ potassium channels in sensory system and neural circuits. *Acta Pharmacol Sin* **37**, 25-33 (2016). https://doi.org/10.1038/aps.2015.131

10 Wang, H. S. *et al.* KCNQ2 and KCNQ3 potassium channel subunits: molecular correlates of the M-channel. *Science* **282**, 1890-1893 (1998). https://doi.org/10.1126/science.282.5395.1890

11 Devaux, J. J., Kleopa, K. A., Cooper, E. C. & Scherer, S. S. KCNQ2 is a nodal K+ channel. *J Neurosci* **24**, 1236-1244 (2004). https://doi.org/10.1523/JNEUROSCI.4512-03.2004

12 Etxeberria, A., Santana-Castro, I., Regalado, M. P., Aivar, P. & Villarroel, A. Three mechanisms underlie KCNQ2/3 heteromeric potassium M-channel potentiation. *J Neurosci* **24**, 9146-9152 (2004). https://doi.org/10.1523/JNEUROSCI.3194-04.2004

13 Bal, M., Zhang, J., Zaika, O., Hernandez, C. C. & Shapiro, M. S. Homomeric and heteromeric assembly of KCNQ (Kv7) K+ channels assayed by total internal reflection fluorescence/fluorescence resonance energy transfer and patch clamp analysis. *J Biol Chem* **283**, 30668-30676 (2008). https://doi.org/10.1074/jbc.M805216200

14 Soh, H., Springer, K., Doci, K., Balsbaugh, J. L. & Tzingounis, A. V. KCNQ2 and KCNQ5 form heteromeric channels independent of KCNQ3. *Proc Natl Acad Sci U S A* **119**, e2117640119 (2022). https://doi.org/10.1073/pnas.2117640119

15 Varghese, N. *et al.* KCNQ2/3 Gain-of-Function Variants and Cell Excitability: Differential Effects in CA1 versus L2/3 Pyramidal Neurons. *J Neurosci* **43**, 6479-6494 (2023). https://doi.org/10.1523/JNEUROSCI.0980-23.2023

16 Doyle, D. A. *et al.* The structure of the potassium channel: molecular basis of K+ conduction and selectivity. *Science* **280**, 69-77 (1998). https://doi.org/10.1126/science.280.5360.69

17 Sun, J. & MacKinnon, R. Cryo-EM Structure of a KCNQ1/CaM Complex Reveals Insights into Congenital Long QT Syndrome. *Cell* **169**, 1042-1050 e1049 (2017).

https://doi.org/10.1016/j.cell.2017.05.019

18 Wu, X., Perez, M. E., Noskov, S. Y. & Larsson, H. P. A general mechanism of KCNE1 modulation of KCNQ1 channels involving non-canonical VSD-PD coupling. *Commun Biol* **4**, 887 (2021). https://doi.org/10.1038/s42003-021-02418-1

19 Huang, J., Pan, X. & Yan, N. Structural biology and molecular pharmacology of voltage-gated ion channels. *Nat Rev Mol Cell Biol* **25**, 904-925 (2024). https://doi.org/10.1038/s41580-024-00763-7

20 Sun, J. & MacKinnon, R. Structural Basis of Human KCNQ1 Modulation and Gating. *Cell* **180**, 340-347 e349 (2020). https://doi.org/10.1016/j.cell.2019.12.003

21 Li, T. *et al.* Structural Basis for the Modulation of Human KCNQ4 by Small-Molecule Drugs. *Mol Cell* **81**, 25-37 e24 (2021). https://doi.org/10.1016/j.molcel.2020.10.037

22 Li, X. *et al.* Molecular basis for ligand activation of the human KCNQ2 channel. *Cell Res* **31**, 52-61 (2021). https://doi.org/10.1038/s41422-020-00410-8

23 Zheng, Y. *et al.* Structural insights into the lipid and ligand regulation of a human neuronal KCNQ channel. *Neuron* **110**, 237-247 e234 (2022). https://doi.org/10.1016/j.neuron.2021.10.029

24 Ma, D. *et al.* Ligand activation mechanisms of human KCNQ2 channel. *Nat Commun* **14**, 6632 (2023). https://doi.org/10.1038/s41467-023-42416-x

25 Zhang, S. *et al.* A small-molecule activation mechanism that directly opens the KCNQ2 channel. *Nat Chem Biol* **20**, 847-856 (2024). https://doi.org/10.1038/s41589-023-01515-y

26 Li, J. *et al.* Small molecule inhibits KCNQ channels with a non-blocking mechanism. *Nat Chem Biol* **21**, 1100-1109 (2025). https://doi.org/10.1038/s41589-024-01834-8

27 Yang, Z. *et al.* Phosphatidylinositol 4,5-bisphosphate activation mechanism of human KCNQ5. *Proc Natl Acad Sci U S A* **122**, e2416738122 (2025). https://doi.org/10.1073/pnas.2416738122

28 Kasuya, G. & Nakajo, K. Optimized tight binding between the S1 segment and KCNE3 is required for the constitutively open nature of the KCNQ1-KCNE3 channel complex. *Elife* **11** (2022). https://doi.org/10.7554/eLife.81683

29 Cui, C. *et al.* Mechanisms of KCNQ1 gating modulation by KCNE1/3 for cell-specific function. *Cell Res* (2025). https://doi.org/10.1038/s41422-025-01152-1

30 Ambrosino, P. *et al.* Epilepsy-causing mutations in Kv7.2 C-terminus affect binding and functional modulation by calmodulin. *Biochim Biophys Acta* **1852**, 1856-1866 (2015). https://doi.org/10.1016/j.bbadis.2015.06.012

31 Bernardo-Seisdedos, G. *et al.* Structural basis and energy landscape for the Ca(2+) gating and calmodulation of the Kv7.2 K(+) channel. *Proc Natl Acad Sci U S A* **115**, 2395-2400 (2018). https://doi.org/10.1073/pnas.1800235115

32 Chang, A. *et al.* A Calmodulin C-Lobe Ca(2+)-Dependent Switch Governs Kv7 Channel Function. *Neuron* **97**, 836-852 e836 (2018). https://doi.org/10.1016/j.neuron.2018.01.035

33 Zaydman, M. A. & Cui, J. PIP2 regulation of KCNQ channels: biophysical and molecular mechanisms for lipid modulation of voltage-dependent gating. *Front Physiol* **5**, 195 (2014). https://doi.org/10.3389/fphys.2014.00195

34 Choveau, F. S., De la Rosa, V., Bierbower, S. M., Hernandez, C. C. & Shapiro, M. S. Phosphatidylinositol 4,5-bisphosphate (PIP(2)) regulates KCNQ3 K(+) channels by interacting with four cytoplasmic channel domains. *J Biol Chem* **293**, 19411-19428 (2018). https://doi.org/10.1074/jbc.RA118.005401

35 Brueggemann, L. I., Mackie, A. R., Martin, J. L., Cribbs, L. L. & Byron, K. L. Diclofenac distinguishes

among homomeric and heteromeric potassium channels composed of KCNQ4 and KCNQ5 subunits. *Mol Pharmacol* **79**, 10-23 (2011). https://doi.org/10.1124/mol.110.067496

36 Nissenkorn, A. *et al.* Donepezil as a new therapeutic potential in KCNQ2- and KCNQ3-related autism. *Front Cell Neurosci* **18**, 1380442 (2024). https://doi.org/10.3389/fncel.2024.1380442

37 Schubert-Bast, S. *et al.* Sodium channel blockers in KCNQ2-encephalopathy: Lacosamide as a new treatment option. *Seizure* **51**, 171-173 (2017). https://doi.org/10.1016/j.seizure.2017.08.005

38 Goto, A. *et al.* Characteristics of KCNQ2 variants causing either benign neonatal epilepsy or developmental and epileptic encephalopathy. *Epilepsia* **60**, 1870-1880 (2019). https://doi.org/10.1111/epi.16314

39 Biervert, C. *et al.* A potassium channel mutation in neonatal human epilepsy. *Science* **279**, 403-406 (1998). https://doi.org/10.1126/science.279.5349.403

40 Singh, N. A. *et al.* A novel potassium channel gene, KCNQ2, is mutated in an inherited epilepsy of newborns. *Nat Genet* **18**, 25-29 (1998). https://doi.org/10.1038/ng0198-25

41 Allen, N. M. *et al.* The variable phenotypes of KCNQ-related epilepsy. *Epilepsia* **55**, e99-105 (2014). https://doi.org/10.1111/epi.12715

42 Allen, N. M., Weckhuysen, S., Gorman, K., King, M. D. & Lerche, H. Genetic potassium channel-associated epilepsies: Clinical review of the K(v) family. *Eur J Paediatr Neurol* **24**, 105-116 (2020). https://doi.org/10.1016/j.ejpn.2019.12.002

43 Vanoye, C. G. *et al.* High-throughput evaluation of epilepsy-associated KCNQ2 variants reveals functional and pharmacological heterogeneity. *JCI Insight* **7** (2022). https://doi.org/10.1172/jci.insight.156314

44 Beacher, N. G., Brodie, M. J. & Goodall, C. A case report: retigabine induced oral mucosal dyspigmentation of the hard palate. *BMC Oral Health* **15**, 122 (2015). https://doi.org/10.1186/s12903-015-0102-y

45 Clark, S., Antell, A. & Kaufman, K. New antiepileptic medication linked to blue discoloration of the skin and eyes. *Ther Adv Drug Saf* **6**, 15-19 (2015). https://doi.org/10.1177/2042098614560736

46 Namdari, R., Luzon, C., Cadieux, J. A., Leung, J. & Beatch, G. N. Pharmacokinetics of XEN496, a Novel Pediatric Formulation of Ezogabine, Under Fed and Fasted Conditions: A Phase 1 Trial. *Neurol Ther* **11**, 781-796 (2022). https://doi.org/10.1007/s40120-022-00343-x

47 French, J. A. *et al.* Efficacy and Safety of XEN1101, a Novel Potassium Channel Opener, in Adults With Focal Epilepsy: A Phase 2b Randomized Clinical Trial. *JAMA Neurol* **80**, 1145-1154 (2023). https://doi.org/10.1001/jamaneurol.2023.3542

48 Yang, G. M. *et al.* Functional characterization and in vitro pharmacological rescue of KCNQ2 pore mutations associated with epileptic encephalopathy. *Acta Pharmacol Sin* **44**, 1589-1599 (2023). https://doi.org/10.1038/s41401-023-01073-y

49 Lattanzi, S. *et al.* A profile of azetukalner for the treatment of epilepsy: from pharmacology to potential for therapy. *Expert Rev Clin Pharmacol* **17**, 423-432 (2024). https://doi.org/10.1080/17512433.2024.2337012

50 Boehlen, A. *et al.* The new KCNQ2 activator 4-Chlor-N-(6-chlor-pyridin-3-yl)-benzamid displays anticonvulsant potential. *Br J Pharmacol* **168**, 1182-1200 (2013). https://doi.org/10.1111/bph.12065

51 Filareto, I. *et al.* Pharmacological approaches in drug-resistant pediatric epilepsies caused by pathogenic variants in potassium channel genes. *Front Cell Neurosci* **18**, 1512365 (2024). https://doi.org/10.3389/fncel.2024.1512365

52 Gomez-Posada, J. C. *et al.* A pore residue of the KCNQ3 potassium M-channel subunit controls surface expression. *J Neurosci* **30**, 9316-9323 (2010). https://doi.org/10.1523/JNEUROSCI.0851-10.2010

53 Zaika, O., Hernandez, C. C., Bal, M., Tolstykh, G. P. & Shapiro, M. S. Determinants within the turret and pore-loop domains of KCNQ3 K+ channels governing functional activity. *Biophys J* **95**, 5121-5137 (2008). https://doi.org/10.1529/biophysj.108.137604

54 Whiffin, N. *et al.* CardioClassifier: disease- and gene-specific computational decision support for clinical genome interpretation. *Genet Med* **20**, 1246-1254 (2018). https://doi.org/10.1038/gim.2017.258

55 Martin, H. C. *et al.* Clinical whole-genome sequencing in severe early-onset epilepsy reveals new genes and improves molecular diagnosis. *Hum Mol Genet* **23**, 3200-3211 (2014). https://doi.org/10.1093/hmg/ddu030

56 Tatulian, L., Delmas, P., Abogadie, F. C. & Brown, D. A. Activation of expressed KCNQ potassium currents and native neuronal M-type potassium currents by the anti-convulsant drug retigabine. *J Neurosci* **21**, 5535-5545 (2001). https://doi.org/10.1523/JNEUROSCI.21-15-05535.2001

57 Kim, K. S., Duignan, K. M., Hawryluk, J. M., Soh, H. & Tzingounis, A. V. The Voltage Activation of Cortical KCNQ Channels Depends on Global PIP2 Levels. *Biophys J* **110**, 1089-1098 (2016). https://doi.org/10.1016/j.bpj.2016.01.006

58 Bialer, M. *et al.* Progress report on new antiepileptic drugs: A summary of the Sixteenth Eilat Conference on New Antiepileptic Drugs and Devices (EILAT XVI): II. Drugs in more advanced clinical development. *Epilepsia* **63**, 2883-2910 (2022). https://doi.org/10.1111/epi.17376

59 Punjani, A., Rubinstein, J. L., Fleet, D. J. & Brubaker, M. A. cryoSPARC: algorithms for rapid unsupervised cryo-EM structure determination. *Nat Methods* **14**, 290-296 (2017). https://doi.org/10.1038/nmeth.4169

60 Bepler, T. *et al.* Positive-unlabeled convolutional neural networks for particle picking in cryo-electron micrographs. *Nat Methods* **16**, 1153-1160 (2019). https://doi.org/10.1038/s41592-019-0575-8

61 Emsley, P., Lohkamp, B., Scott, W. G. & Cowtan, K. Features and development of Coot. *Acta Crystallogr D Biol Crystallogr* **66**, 486-501 (2010). https://doi.org/10.1107/S0907444910007493

62 Afonine, P. V. *et al.* Towards automated crystallographic structure refinement with phenix.refine. *Acta Crystallogr D Biol Crystallogr* **68**, 352-367 (2012). https://doi.org/10.1107/S0907444912001308

63 Croll, T. I. ISOLDE: a physically realistic environment for model building into low-resolution electron-density maps. *Acta Crystallogr D Struct Biol* **74**, 519-530 (2018). https://doi.org/10.1107/S2059798318002425

64 Pettersen, E. F. *et al.* UCSF ChimeraX: Structure visualization for researchers, educators, and developers. *Protein Sci* **30**, 70-82 (2021). https://doi.org/10.1002/pro.3943

Acknowledgements

We thank the Structural Biology and Biomedical Electrophysiology Core Facilities at the Bio-Tech Center, as well as the Biomedical Data Center, of Shenzhen Medical Academy of Research and Translation (SMART) for their technical support and experimental assistance. We are grateful to Dr. Kun Wu at the SMART-SZBL Rare Disease Center for providing information on KCNQ-related disease mutations. This work was funded by the National Natural Science Foundation of China (32501082 to J.H.). J.H. and X.F. are also supported by the start-up funding from Shenzhen Medical Academy of Research and Translation (SMART).

Author Contributions

J.H. conceived the project. F.L., X.H., G.C., Y.X., X.F., and J.H. designed experiments; F.L., X.H., and Y.X. carried out experiments related to cryo-EM studies, including protein expression, purification, and data acquisition; X.F. performed data processing; G.C. conducted experiments related to electrophysiology; F.L., X.H., G.C., Y.X., X.F., and J.H. analyzed data; F.L., X.H., X.F., and J.H. wrote the manuscript with input from all authors. All authors approved the final manuscript.

Competing Interest

The authors declare no competing interests.

Figures and Figure Legends

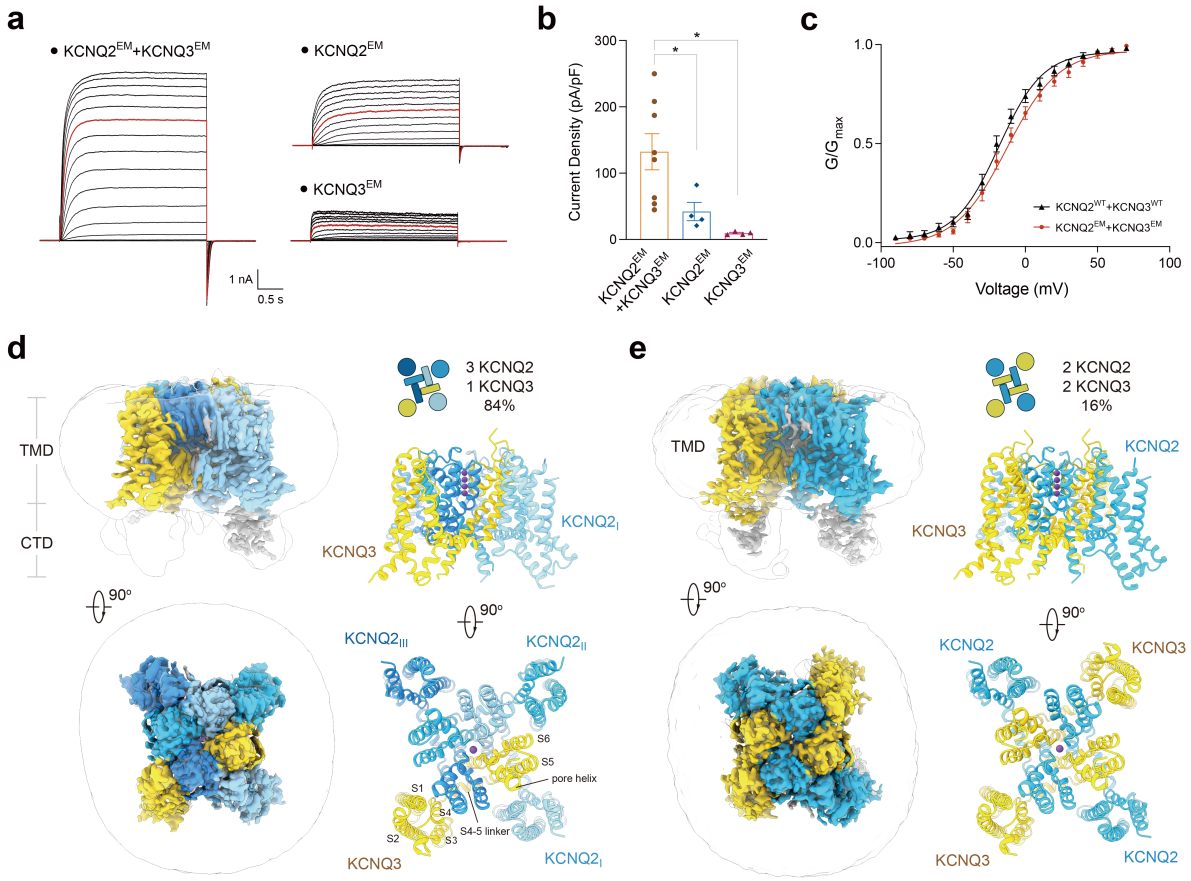

Fig. 1 | Overall architecture of human M-channels with two distinct stoichiometries. **a,** Representative whole-cell currents recorded from HEK293T cells expressing heteromeric KCNQ2/KCNQ3 channels (*left*), KCNQ2 (*upper right*), or KCNQ3 (*lower right*). Co-expression generated larger currents than either subunit alone. Currents were elicited from -90 mV and stepped to +70 mV for 1500 ms. Truncated constructs used for structural determination are denoted as EM. **b,** Quantification of current densities: 132.27 ± 27.18 pA/pF for KCNQ2+KCNQ3, 42.17 ± 13.65 pA/pF for KCNQ2, and 9.44 ± 1.20 pA/pF for KCNQ3 (n = 8, 4, 4; mean ± SEM). **c,** Voltage-dependent activation of heteromeric KCNQ2/KCNQ3 channels. Truncated constructs ($KCNQ2^{EM}$+$KCNQ3^{EM}$, $V_{1/2}$ = -12.84 ± 1.26 mV, n = 7) exhibited activation properties comparable to full-length channels

($KCNQ2^{WT}$+$KCNQ3^{WT}$, $V_{1/2}$ = -18.19 ± 1.16 mV, n = 10). Please refer to Methods for experimental details. **d-e,** Cryo-EM structures of human M-channels resolved in two stoichiometries. The predominant assembly (84%) adopts an asymmetric 3:1 stoichiometry of KCNQ2 to KCNQ3 (**d**), while a minor population (16%) forms a staggered 2:2 stoichiometry (**e**). Shown here are side and extracellular views of cryo-EM density maps and atomic models, with KCNQ3 colored in yellow and KCNQ2 in blue. For clarity, KCNQ2 subunits in the asymmetric assembly are labeled $KCNQ2_{I}$, $KCNQ2_{II}$, and $KCNQ2_{III}$, ordered counterclockwise from KCNQ3 in the extracellular view. All structural figures were prepared in ChimeraX[64].

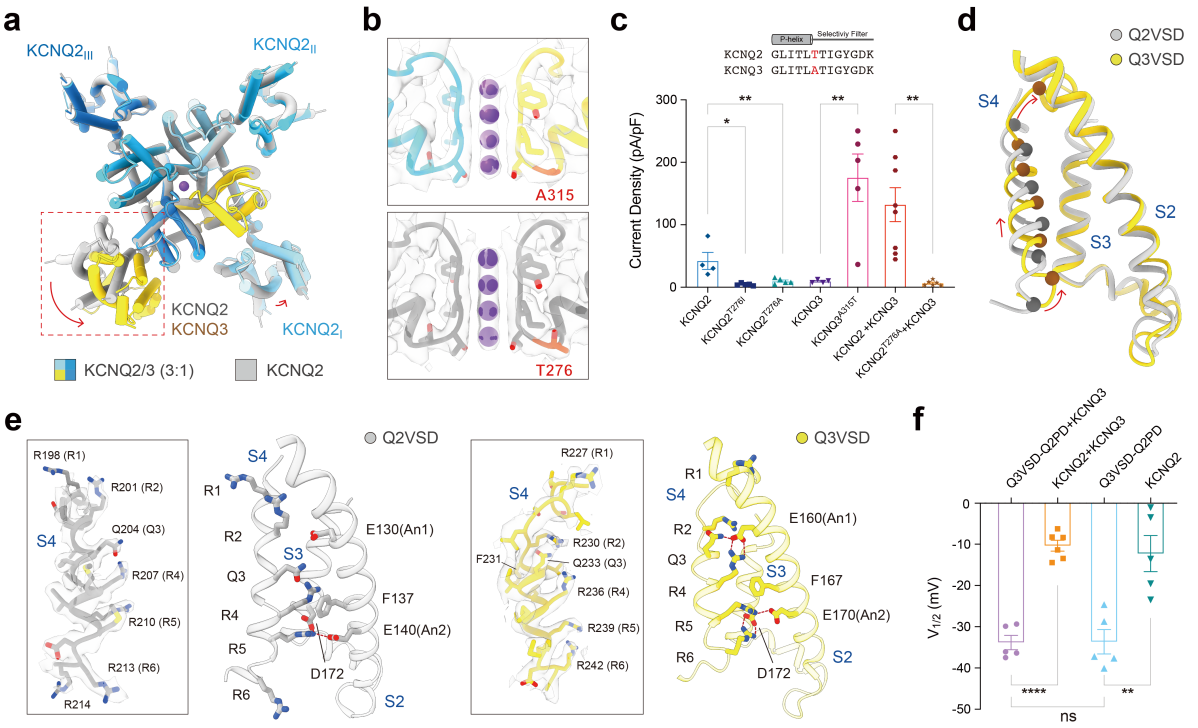

Fig. 2 | KCNQ3 confers low-voltage activation to human M-channels. **a,** Structural comparison of the transmembrane regions of the heteromeric M-channel (3:1) and homotetrameric KCNQ2. Shown here are superimposed structures of the M channel (domain colored) and KCNQ2 (gray), with transmembrane helices depicted as cylinders. The KCNQ3 subunit exhibits a pronounced counterclockwise rotation of the entire VSD when viewed from the extracellular side. **b,** Close-up view of the selectivity filter (SF) with superimposed EM densities, with bound K^+ ions indicated in purple. KCNQ3 harbors a unique Ala residue immediately preceding SF, distinct from KCNQ2. **c,** Functional analysis of the critical Ala residue in KCNQ3. Values of current density are 4.39 ± 1.85 pA/pF for $KCNQ2^{T276I}$, 9.78 ± 1.93 pA/pF for $KCNQ2^{T276A}$, 175.41 ± 37.98 pA/pF for $KCNQ3^{A315T}$, 6.54 ± 1.59 pA/pF for $KCNQ2^{T276A}$+KCNQ3 (n = 5, 5, 5, 6; mean ± SEM). The sequence alignment shown above highlights the unique Ala position in KCNQ3. **d,** Distinct VSD conformation in KCNQ3. Superimposed VSDs show that the S4 helix of KCNQ3 adopts an ‘up’ conformation

compared to that of KCNQ2. **e,** Comparison of VSD structures in KCNQ2 and KCNQ3. Gating charge (GC) residues on S4 and conserved acidic/polar residues (An1, An2) on S2 are shown as sticks. *Inset*: EM density of the S4 helix in KCNQ3, revealing an elongated loop spanning Arg227-Phe231, rather than the helical turn present in KCNQ2. **f,** Electrophysiological characterization of the KCNQ3 VSD confirming its contribution to the low-threshold activation of M-channels. $V_{1/2}$ values are -33.85 ± 0.67 mV for Q3VSD-Q2PD+KCNQ3, -12.84 ± 1.26 mV for KCNQ2+KCNQ3, -35.32 ± 1.71 mV for Q3VSD-Q2PD alone, and -12.16 ± 2.49 mV for KCNQ2 alone (n = 5, 6, 5, 5; mean ± SEM).

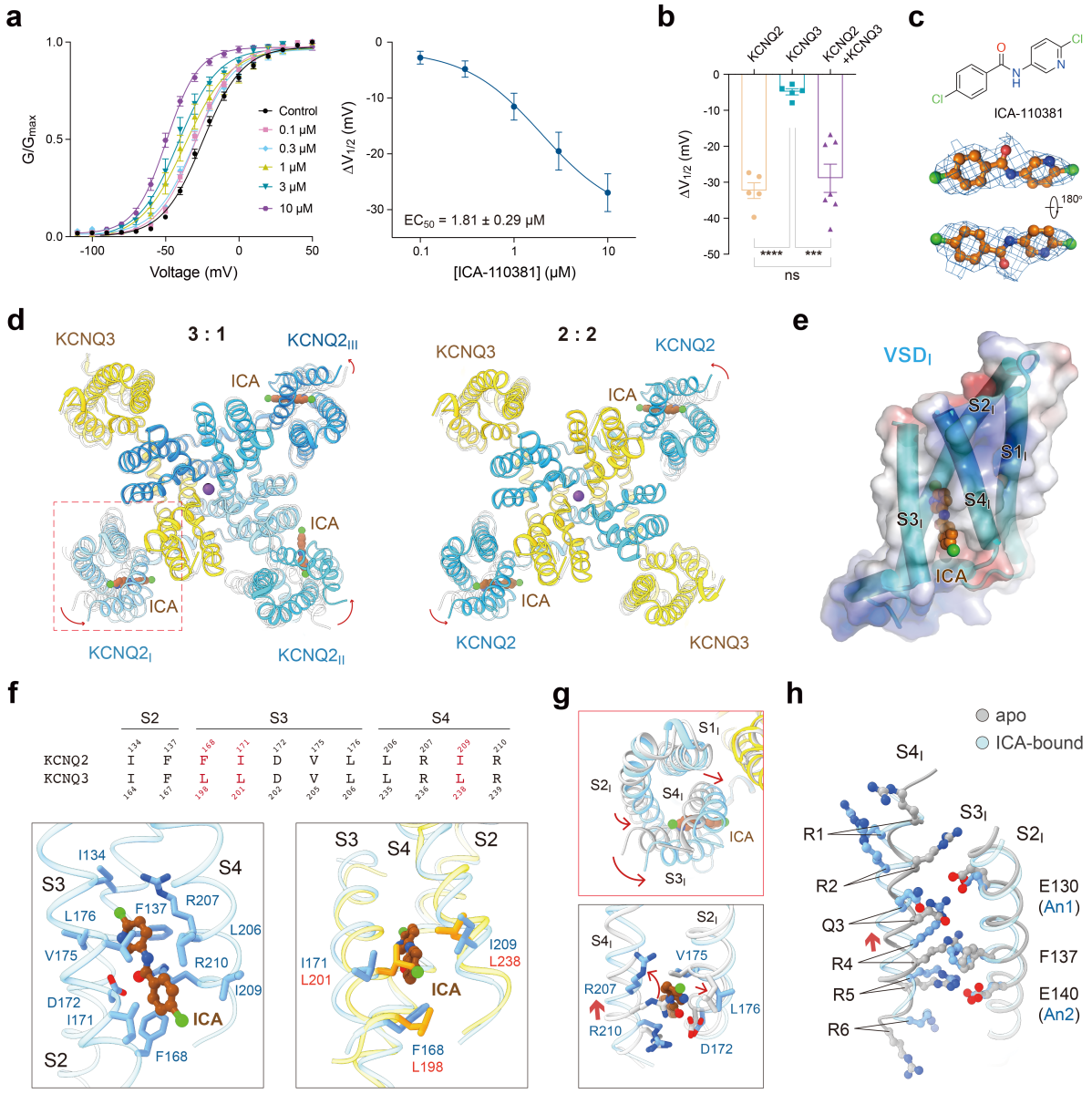

Fig. 3 | ICA-110381 selectively activates the M-channels via KCNQ2 VSDs. **a,** Electrophysiological analysis of ICA-110381 effects on the M-channels. *Left*: Normalized activation curves recorded in the presence of increasing ICA-110381 concentrations. *Right*: Dose-dependent response of ICA-110381-induced activation shifts, with the EC_{50} value of 1.81 ± 0.29 μM. **b,** Effects of 10 μM ICA-110381 on channel activation. $\Delta V_{1/2}$ values are -28.76 ± 3.92 mV for KCNQ2/3, -32.20 ± 2.19 mV for KCNQ2, and -4.71 ± 0.86 mV for KCNQ3 (n = 7, 5, 5; mean ± SEM). **c,** Chemical structure and corresponding EM density of

ICA-110381. **d,** Selective binding of ICA-110381 to KCNQ2 VSDs. Shown here are the extracellular views of M-channels in complex with ICA-110381 at different stoichiometries. Superimposed apo (gray) and activator-bound (domain-colored) structures highlight local conformation changes, as indicated by red arrows. **e,** Electrostatic surface of the KCNQ2 VSD with ICA-110381 bound, shown as ball-and-sticks. **f,** Structural determinants of subtype selectivity. *Top*: Structure-guided sequence comparison of binding residues, with KCNQ2- or KCNQ3-specific positions highlighted in red. *Bottom*: Detailed coordination of ICA-110381 within the KCNQ2 VSD, with unique residues indicated. **g,** Conformational rearrangements of the KCNQ2 VSD upon ICA-110381 binding. Shown here are the superimposed apo- (gray) and ICA-110381-bound (light blue) structures, with the local shifts indicated by red arrows. **h,** ICA-110381 stabilizes an ‘up’ VSD. Gating charge (GC) residues on S4 and conserved acidic/polar residues (An1, An2) on S2 are shown as sticks, with displacement directions highlighted by red arrows.

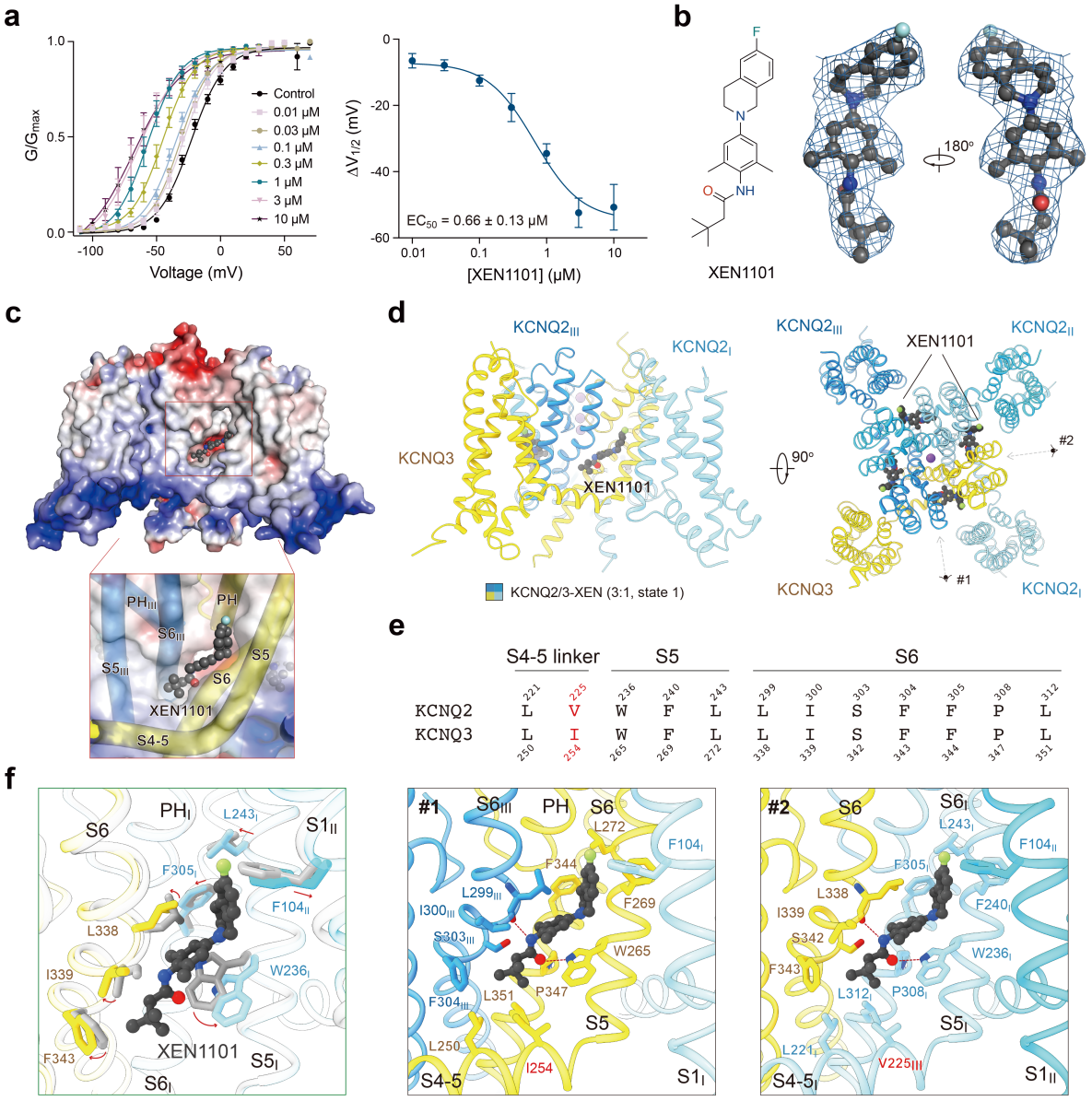

Fig. 4 | PD-targeting activation of the M-channel by XEN1101. **a,** Electrophysiological analysis of XEN1101 effects on heteromeric M-channels. *Left*: Normalized voltage-dependent activation curves at increasing XEN1101 concentrations. *Right*: Dose-dependent response of XEN1101-induced activation shifts, with the EC_{50} value of 0.66 ± 0.13 μM. **b,** Chemical structure and corresponding EM density of XEN1101. **c,** Electrostatic surface of the M-channel transmembrane region in complex with XEN1101. *Inset*: XEN1101 binds to the fenestration formed by the adjacent PDs from different subunits. **d,** Binding of four

XEN1101 molecules to distinct fenestrations. Shown here are the side and extracellular views of XEN1101-bound M-channel. Despite two molecules of XEN1101 binding to the KCNQ2-KCNQ2 interface, the other two bind to the heterotypic sites contributed by KCNQ3 (labeled #1 and #2). **e,** Conservation of the XEN1101-binding pocket between KCNQ2 and KCNQ3. *Top*: Structure-guided sequence alignment of binding residues with subtype-specific positions highlighted in red. *Bottom*: Detailed coordination of XEN1101 at KCNQ3-containing fenestrations, with unique residues indicated by red. **f,** Local conformation rearrangements induced by XEN1101. Shown here are superimposed apo- (gray) and XEN1101-bound (domain-colored) structures, with structural shifts indicated by red arrows.

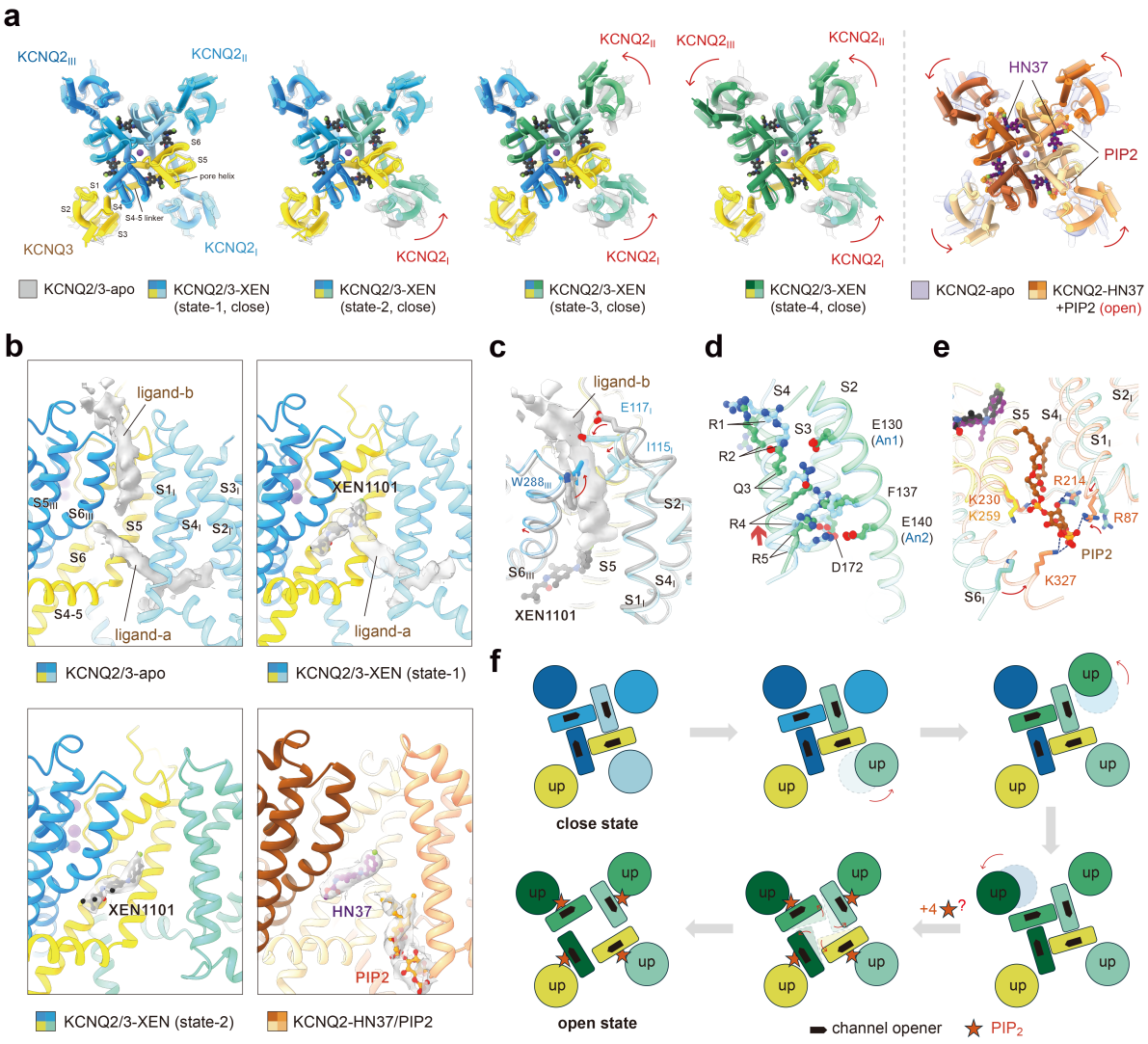

Fig. 5 | Cooperative gating of human M-channels by pore-targeting modulators and PIP$_2$. **a,** KCNQ2 VSDs adopt multiple conformations in the presence of XEN1101. Four distinct states were resolved from a single dataset: State-1 with three 'down' KCNQ2 VSDs, State-2 with one 'up' KCNQ2 VSD, State-3 with two 'up' KCNQ2 VSDs, and State-4 with all 'up' VSDs. Shown here are superimposed structures of each state (domain-colored) aligned with the apo channel (gray). For comparison, the open KCNQ2 structure bound to another pore-targeting opener, HN37, along with PIP$_2$, is shown on the *right*, with similar VSD displacements indicated by red arrows. **b,** Ligand occupancy at the PD-VSD interface across states. In the apo channel, the KCNQ2 VSD-PD interface engages two unknown

ligands, designated as ligand-a (on the intracellular side) and ligand-b (on the extracellular side). With XEN1101 bound, only ligand-a remains at interfaces containing 'down' VSDs, while PDs adjacent to 'up' VSDs are engaged solely by XEN1101. In the presence of both HN37 and PIP_2, the PD-VSD interface is additionally occupied by a well-resolved PIP_2 density. **c-e,** Structural transitions between states. The binding of XEN1101 introduces steric clashes with the ligand-b density (**c**). VSD rearrangements accompanying the 'down-to-up' transition mimic those observed in KCNQ3, as described in Fig. 2 (**d**). PIP_2 binding reinforces coupling between the VSD and S6 helix, thereby promoting channel opening (**e**). **f,** Schematic of cooperative gating. Sequential counterclockwise rotation of adjacent KCNQ2 VSDs, viewed from the extracellular side, progressively creates space for PIP_2 binding, which, together with pore-targeting activators, drives channel opening.